The Astrophysical Journal, 998:218 (12pp), 2026 February 20 https://doi.org/10.3847/1538-4357/ae33bb

Fluctuation Dynamos in Supersonic Turbulence at Pm $\gtrsim$ 1

Ameya Uday Nagdeo[1,2], Sharanya Sur[1,2], and Bhargav Vaidya[3]
[1] Indian Institute of Astrophysics, 2nd Block, Koramangala, Bangalore 560034, India; ameya.nagdeo@iiap.res.in
[2] Affiliated to Pondicherry University, R.V. Nagar, Kalapet, Puducherry, 605014, India
[3] Indian Institute of Technology-Indore, Simrol, 452020, India
Received 2025 September 8; revised 2026 January 1; accepted 2026 January 2; published 2026 February 11

Abstract

Fluctuation dynamos provide a robust mechanism for amplifying weak seed magnetic fields in turbulent astrophysical plasmas. However, their behaviour in the highly compressible regimes characteristic of the interstellar medium remains incompletely understood. Using high-resolution 3D magnetohydrodynamic simulations of supersonic turbulence with rms Mach number $\mathcal{M}_{\rm rms} \approx 11$, we explore fluctuation dynamos across magnetic Prandtl numbers Pm = 1–10. At Pm = 1, dynamo growth is slower and saturates at lower magnetic-to-kinetic energy ratios, with amplification in the kinematic phase dominated by compression rather than line stretching. In contrast, at Pm = 10, vortical stretching emerges as the dominant mechanism, yielding faster growth, higher saturation levels, and stronger suppression of density–magnetic field correlations by magnetic pressure. This transition is reflected in the correlation coefficient between density and magnetic field strength, which is strongly positive at Pm = 1 but decreases significantly at higher Pm. Across all runs, the ratio of velocity-to-magnetic integral scales is ∼3.4, in the saturated phase, independent of Pm, while the ratio of viscous to resistive dissipation scales increases with the increase in Pm. Synthetic Faraday rotation measures reveal coherence lengths of ∼one-fourth to one-third of the forcing scale across the range of Pm explored. Using these coherence scales, we discuss the potential contribution of fluctuation dynamos to Faraday rotation expected from turbulent, gas-rich young disk galaxies.

Unified Astronomy Thesaurus concepts: Magnetohydrodynamics (1964); Interstellar magnetic fields (845); Magnetohydrodynamical simulations (1966)

1. Introduction

Magnetic fields are a fundamental component of nearly all astrophysical systems, from stars and galaxies to the intracluster medium. Their ubiquity and persistence are widely attributed to dynamo processes, which amplify and sustain magnetic fields over cosmic timescales. Among these, the fluctuation dynamo plays a key role in turbulent environments, where it harnesses energy from 3D random/turbulent motions to efficiently amplify weak seed fields to dynamically significant strengths on timescales shorter than the lifetimes of such systems (A. P. Kazantsev 1968; F. Rincon 2019; A. M. Shukurov & K. Subramanian 2021; A. A. Schekochihin 2022). This process is particularly relevant in astrophysical settings dominated by turbulent, conducting plasma such as star-forming regions in galaxies and galaxy clusters (e.g., N. E. Haugen et al. 2004; A. A. Schekochihin et al. 2004; J. Cho et al. 2009; C. Federrath et al. 2011a; P. Bhat & K. Subramanian 2013; C. Federrath 2016; S. Xu & A. Lazarian 2016, 2021; A. Seta et al. 2020; S. Sur & K. Subramanian 2024; N. Kriel et al. 2025). Understanding fluctuation dynamos is essential for unraveling the origin and evolution of cosmic magnetism from the magnetic fields in the first stars (S. Sur et al. 2010, 2012; C. Federrath et al. 2011b) and in the present-day interstellar and intracluster media (e.g., P. Bhat & K. Subramanian 2013; R. Pakmor et al. 2017; J. Donnert et al. 2018; F. Marinacci et al. 2018; A. M. Shukurov & K. Subramanian 2021) to the observational evidence for magnetization in high-redshift galaxies (e.g., M. L. Bernet et al. 2008; J. S. Farnes et al. 2014; J. E. Geach et al. 2023; J. Chen et al. 2024).

Fluctuation dynamos amplify magnetic fields through the competition between inductive growth and resistive dissipation. Sustained amplification requires that induction dominates over diffusion, which occurs only when the magnetic Reynolds number Rm exceeds a critical threshold, $\mathrm{Rm} > \mathrm{Rm}_{\rm cr}$. From the perspective of numerical simulations, this implies that both inductive and dissipative contributions at individual grid points tend to be significantly larger than their mean values. This is clearly reflected in the broad probability distribution functions (PDFs) presented in S. Sur & K. Subramanian (2024), where the standard deviation notably exceeds the mean of the PDFs. Indeed, it is the volume-integrated balance of these opposing effects that ultimately determines whether the magnetic field experiences net growth or decay.

In this study, we explore fluctuation dynamos operating in the regime of supersonic turbulence—conditions highly representative of the interstellar medium (ISM) in galaxies. Supersonic flows introduce strong compressibility and shock-driven structures that can fundamentally influence the dynamics of turbulent magnetic field amplification (A. G. Kritsuk et al. 2007; C. Federrath et al. 2011a, 2016; A. Seta & C. Federrath 2021a; F. A. Gent et al. 2023; J. R. Beattie et al. 2024; S. Sur & K. Subramanian 2024). These effects are especially pertinent in the context of early galaxy evolution and high-redshift environments, where the ISM is likely to be more dynamic, denser, and more turbulent than in present-day spiral galaxies (e.g., A. W. Green et al. 2010; F. Bournaud et al. 2011; K. Kraljic et al. 2024; F. Rizzo et al. 2024). Fluctuation dynamos are expected to play a central role in such settings,

acting as efficient mechanisms for the rapid amplification of magnetic fields from weak initial seed values. These small-scale fields may not only catalyze the growth of the large-scale, coherent galactic magnetic fields observed today but could also actively facilitate their development by expelling small-scale magnetic helicity through helicity fluxes (e.g., K. Gopalakrishnan & K. Subramanian 2023; A. Brandenburg & E. T. Vishniac 2025, among recent works). Thus, understanding fluctuation dynamos in the supersonic regime forms a key component in understanding galactic magnetic fields.

We specifically explore the fluctuation dynamo in supersonic turbulence with rms Mach number $\mathcal{M}_{\rm rms} \approx 11$, focusing on magnetic Prandtl numbers Pm $=$ Rm/Re$=\nu/\eta \gtrsim 1$, with cases explored up to Pm $= 10$. Here, Rm and Re denote the magnetic and fluid Reynolds numbers, while ν and η are the kinematic viscosity and magnetic diffusivity, respectively. Probing the Pm > 1 regime is particularly relevant for the ISM, as such systems are expected to have Pm $\gg 1$, with estimates for the warm diffuse phase reaching Pm $\sim 10^{10}$–10^{14} (A. Brandenburg & K. Subramanian 2005; J. Schober et al. 2012). However, we restrict our exploration to Pm $\leqslant 10$ to maintain computational feasibility. Within this parameter space, we seek to address some fundamental questions from the perspective of the Pm $= 1$ and Pm > 1 regimes. By contrasting these two regimes, we first explore how Pm influences the growth rate and saturation levels of magnetic energy. Next, how does the correlation between density and magnetic field strength evolve across different Pm values, and what roles do the weak and strong field regions play in shaping this correlation? We further investigate the balance between local stretching and compression during the saturated phase of the dynamo and assess the resulting magnetic field coherence using synthetic Faraday rotation measures (RMs). Together, these analyses provide new insights into the nature and efficiency of fluctuation dynamos.

The paper is structured as follows. Section 2 details the numerical setup, including initial and boundary conditions. Section 3 presents visualizations of density and magnetic field strengths, along with the time evolution of $\mathcal{M}_{\rm rms}$ and the magnetic-to-kinetic energy ratios. In Section 4, we examine the correlation between density and magnetic field strengths, highlighting differences across weak and strong field regions. Section 5 discusses the power spectra and characteristic length scales, such as the integral and dissipation scales of the velocity and magnetic fields. Using the magnetic energy evolution as a starting point, Section 6 investigates the roles of local stretching and compression and their dependence on Pm. Section 7 is devoted to an analysis of the Faraday RM obtained from the dynamo-generated fields in the different physical regimes quantified by the varying Pm. Finally, in Section 8, we summarize the key findings and discuss their implications.

2. Numerical Simulations

We perform nonideal magnetohydrodynamic (MHD) simulations of fluctuation dynamos in supersonic flows in three dimensions using a newly developed driven turbulence module in PLUTO (A. Mignone et al. 2007),[4] which is a widely used, finite-volume, astrophysical MHD code. The simulations were performed in dimensionless coordinates with a cubic box of unit length ($L = 1$) at 512^3 resolution. The dimensionless density (ρ) and sound speed ($c_{\rm s}$) are initialized with $\rho = 1$, $c_{\rm s} = 1$, and zero initial velocities. Adopting an isothermal equation of state, we solve the following set of 3D MHD equations in dimensionless form:

$$\frac{\partial \rho}{\partial t} + \nabla \cdot (\rho \boldsymbol{U}) = 0, \tag{1}$$

$$\frac{\partial (\rho \boldsymbol{U})}{\partial t} + \nabla \cdot (\rho \boldsymbol{U} \otimes \boldsymbol{U} - \boldsymbol{B} \otimes \boldsymbol{B}) + \nabla P^{*} = \nabla \cdot (2\nu\rho \boldsymbol{S}) + \rho \boldsymbol{F}, \tag{2}$$

$$\frac{\partial \boldsymbol{B}}{\partial t} = \nabla \times (\boldsymbol{U} \times \boldsymbol{B}) + \eta \nabla^2 \boldsymbol{B}. \tag{3}$$

Here ρ, $\boldsymbol{U}$, $P^{*} = p + |\boldsymbol{B}|^2/2$, and $\boldsymbol{B}$ represent the fluid density, velocity, total pressure (thermal + magnetic), and magnetic field, respectively, while $\otimes$ denotes the tensor product between vector fields. Furthermore, $S_{ij} = (1/2)[U_{i,j} + U_{j,i} - (2/3)\delta_{ij}\partial_k U_k]$ is the traceless rate of the strain tensor, and $\boldsymbol{F}$ is the turbulent acceleration field modeled using the Ornstein–Uhlenbeck process with a finite time correlation (V. Eswaran & S. B. Pope 1988; D. T. Gillespie 1996; B. Fryxell et al. 2000; R. Benzi et al. 2008; C. Federrath et al. 2010). The viscosity ν and magnetic resistivity η are both treated as constants throughout the simulations.

To regulate solenoidal and compressive contributions in our driven turbulence module, we decompose the acceleration field into solenoidal and compressive components using a projection operator in Fourier space. In index notation, the operator is given by

$$\mathcal{P}^{\zeta}_{ij}(\boldsymbol{k}) = \zeta \mathcal{P}^{\perp}_{ij} + (1 - \zeta)\mathcal{P}^{\parallel}_{ij}, \tag{4}$$

where $\mathcal{P}^{\perp}_{ij}$ and $\mathcal{P}^{\parallel}_{ij}$ are the solenoidal and compressive projection operators, respectively, and $\zeta \in [0, 1]$ is an adjustable parameter that controls the solenoidal contribution. To maximize dynamo efficiency in supersonic turbulence, we use purely solenoidal driving (choosing $\zeta = 1$)[5] in all simulations ensuring $\boldsymbol{k} \cdot \boldsymbol{F}_k = 0$ (k is the wavenumber and $\boldsymbol{F}_k$ is the forcing vector in k-space), exciting only large-scale modes in the range $1 \leqslant |\boldsymbol{k}|L/2\pi \leqslant 3$, with an average forcing wavenumber $k_{\rm f}L/2\pi = 2$, corresponding to a turbulent driving scale $\ell_{\rm f} = 2\pi/k_{\rm f} = L/2$. We further set the correlation time to be the eddy turnover time at this scale, $t_{\rm ed} = \ell_{\rm f}/u_{\rm rms}$, where $u_{\rm rms}$ is the steady-state rms turbulent velocity. The amplitude of the driving is adjusted to yield supersonic turbulence with rms Mach number $\mathcal{M}_{\rm rms} = u_{\rm rms}/c_{\rm s} \approx 11$ when the turbulence is fully developed.

We initialize the setup with a magnetic field $\boldsymbol{B} = B_0[(\sin(15\pi z), 0, 0)]$, where B_0 is chosen so that the initial plasma beta $\beta_{\rm in} = p_{\rm th}/p_{\rm mag} \approx 10^6$ in all the runs; $p_{\rm th}$ and $p_{\rm mag}$ are the thermal and magnetic pressures, respectively. Equations (1)–(3) are then evolved with an explicit time-stepping scheme together with the unsplit staggered mesh MHD Harten, Lax, Van Leer (HLL) solver to compute the fluxes and a constrained transport scheme at the cell interfaces for preserving the divergence-free nature of the magnetic fields ($\nabla \cdot \boldsymbol{B} = 0$) on the staggered grid. We note that even though the ISM exhibits a multiphase structure, the use of an isothermal equation of state enables a cleaner examination of the complex interplay of density fluctuations, turbulence, and

[4] https://plutocode.ph.unito.it/

[5] $\zeta = 0$ implies purely compressive driving, and any value in between implies mixed driving.

Table 1
Key Parameters of the Simulations Used in This Study

Run	Pm	$\mathrm{Re} = u\,\ell_f/\nu$	$\langle E_m/E_k\rangle_{sat}$	$\langle r_p\rangle_{sat}$
Pm1	1	6600	$9.0 \times 10^{-3} \pm 4 \times 10^{-4}$	0.53 ± 0.02
Pm5	5	1320	$3.5 \times 10^{-2} \pm 2 \times 10^{-3}$	0.45 ± 0.01
Pm10	10	660	$8.1 \times 10^{-2} \pm 2 \times 10^{-3}$	0.34 ± 0.01

Note. The resolution in each run is 512^3. $k_f L/2\pi = 2$ is the average forcing wavenumber, and $\mathcal{M}_{rms} \approx 11$ is the average value of the rms Mach number in the steady state. $\ell_f = 2\pi/k_f$ is the forcing scale, and Pm and Re are the magnetic Prandtl number and the fluid Reynolds numbers, respectively. The ratio of the time-averaged magnetic-to-kinetic energies $\langle E_m/E_k\rangle$ and the correlation coefficient $\langle r_p\rangle$ are computed in the saturated state of the dynamo. The $\pm$ values indicate the 1σ standard deviation around the mean.

magnetic fields. To achieve $\mathrm{Pm} = \mathrm{Rm}/\mathrm{Re} = \nu/\eta > 1$, we progressively reduce Re by increasing ν, resulting in $\mathrm{Re} = u_{rms}\ell_f/\nu \approx 6600$, 1320, and 660 for Pm = 1, 5, and 10, respectively. The key simulation parameters are listed in Table 1. For clarity, we will hereafter refer to the different runs as Pm1, Pm5, and Pm10, corresponding to Pm = 1, 5, and 10, respectively.

3. 2D Slices and Time Evolution of the rms Mach Number and Ratio of Energies

In Figure 1, we show the 2D slices of the logarithmic values of the normalized density and magnetic field strengths from Pm1 (top row) and Pm10 (bottom row) in the saturated state of the dynamo. They depict the complex structure of a magnetized, compressible turbulent medium. The left-hand panels visualize $\log(\rho/\langle\rho\rangle)$ using a color map ranging from green (low density, $\log(\rho/\langle\rho\rangle \approx -2.7$) to yellow–white (high density, $\log(\rho/\langle\rho\rangle \approx 1.7$). Here $\langle\rho\rangle \approx 1$ is the mean density in the simulation volume. It is abundantly clear that the supersonic nature of the resulting flows results in sharp density contrasts with high-density structures surrounded by underdense voids. Such structures are hallmark features of compressible turbulence, particularly in supersonic regimes, where shock fronts compress the gas into thin layers.

The right-hand panels show the magnetic field intensity, $\log(B/B_{rms})$, overlaid with vector field arrows representing the in-plane field direction. Blue regions denote weak magnetic fields (sub-rms values), while red regions indicate strong magnetic concentrations exceeding B_{rms}. These slices reveal that, irrespective of the value of Pm, regions with high densities generally correspond to regions with strong magnetic fields, and vice versa, with sub-rms field strengths in the voids. However, a lack of perfect correlation between strong field and high-density regions is also visible in some areas. The arrows of equal length representing the direction of the in-plane fields are seen to be arranged in folds at a number of locations. Some highly dense blobs show ordered magnetic field lines plausibly resulting from compression. This is expected, as in purely solenoidal supersonic turbulence, both compression and random stretching contribute to amplifying the magnetic field through dynamo action (C. Federrath et al. 2011a; C. Federrath 2016; S. Sur et al. 2018; A. Seta & C. Federrath 2021a; S. Sur & K. Subramanian 2024).

The top panel in Figure 2 shows the evolution of the rms Mach number ($\mathcal{M}_{rms}$), while the bottom panel shows the evolution of the ratio of magnetic to kinetic energies (E_m/E_k), both as functions of the normalized time (t/t_{ed}). The behavior of $\mathcal{M}_{rms}$ is shown for three different Pm values: Pm = 1 (blue dashed line), Pm = 5 (red dotted line), and Pm = 10 (solid black line). As seen from the plot, there is an initial transient phase lasting for $\approx 2t/t_{ed}$ beyond which $\mathcal{M}_{rms}$ attains a steady state fluctuating around $\mathcal{M}_{rms} \approx 11$, obtained by averaging from $t/t_{ed} = 5$, until the end of the simulation. The growth of magnetic fields due to dynamo action proceeds in three stages: kinematic, intermediate, and eventual saturation. We find the behavior of the fluctuation dynamo in such highly compressible flows to be sensitive to the relation between the ranges of scales of velocity and magnetic fields, quantified in terms of $\mathrm{Pm} = \nu/\eta$. Notably, the growth rate of the dynamo varies significantly with Pm. In the kinematic phase, these are annotated by slopes in the top left corner of the bottom panel. In Pm1, the growth rate of E_m/E_k is significantly lower ($\gamma \approx 0.42 \pm 0.001$) than Pm5 ($\gamma \approx 0.8 \pm 0.003$) and Pm10 ($\gamma \approx 0.93 \pm 0.002$). This implies that in contrast to Pm = 1, Pm = 10 results in more efficient dynamo action, as the magnetic fields can be amplified on a range of scales ($\ell_\nu > \ell > \ell_\eta$), even by the eddies at the viscous scale. The intermediate phase of growth is particularly prominent in Pm10 extending from $t/t_{ed} = 19$ to 25, while for Pm1 and Pm5, it lasts from $t/t_{ed} = 36$ to 41 and 21 to 28, respectively. In the same vein, we find that the saturation level of E_m depends strongly on the Pm, with the highest level of saturation obtained for Pm10 ($\approx 8 \times 10^{-2}$), which decreases with decreasing Pm (see Table 1). Further, the 1σ uncertainties in the saturated E_m/E_k values reported in Table 1 correspond to only $\sim 4\%-6\%$ of the mean.

4. Correlation between Density and Magnetic Field Strength

In a recent work, S. Sur & K. Subramanian (2024) explored how the Pearson correlation coefficient, $r_p(\rho, B)$, evolves with varying levels of flow compressibility. The coefficient is defined as

$$r_p(\rho, B) = \frac{\mathrm{Cov}(\rho, B)}{\sigma_\rho \sigma_B} = \frac{\sum_{i,j,k}(\rho_{i,j,k} - \langle\rho\rangle)(B_{i,j,k} - \langle B\rangle)}{\sqrt{\sum_{i,j,k}(\rho_{i,j,k} - \langle\rho\rangle)^2}\,\sqrt{\sum_{i,j,k}(B_{i,j,k} - \langle B\rangle)^2}}, \quad (5)$$

where $B = \sqrt{B_x^2 + B_y^2 + B_z^2}$ is the magnitude of the field and $\rho_{i,j,k}$ and $B_{i,j,k}$ are the density and the magnetic field strength at a point (i, j, k) in the simulation volume. $\langle\rho\rangle$ and $\langle B\rangle$ are the mean values of density and B, respectively. One of the key findings from S. Sur & K. Subramanian (2024) was that, in supersonic flows with $\mathcal{M}_{rms} \sim 3$, ρ and B remain positively correlated even in the nonlinear saturated regime, with $\langle r_p\rangle \approx 0.43$. In this study, we further examine the evolution of $r_p(\rho, B)$ across different Pm values in flows with $\mathcal{M}_{rms} \sim 11$.

During the kinematic phase, it is evident from Figure 3 that all three simulations (Pm1, Pm5, and Pm10) exhibit a strong positive correlation with time-averaged $\langle r_p\rangle \approx 0.65$ indicating that initially, higher-density regions are correlated with stronger magnetic fields. However, as the dynamo transitions to the nonlinear saturated phase, r_p starts to decrease. This decline stems from the fact that magnetic field amplification is no longer driven solely by compression; vortical motions arising from solenoidal forcing also contribute significantly to

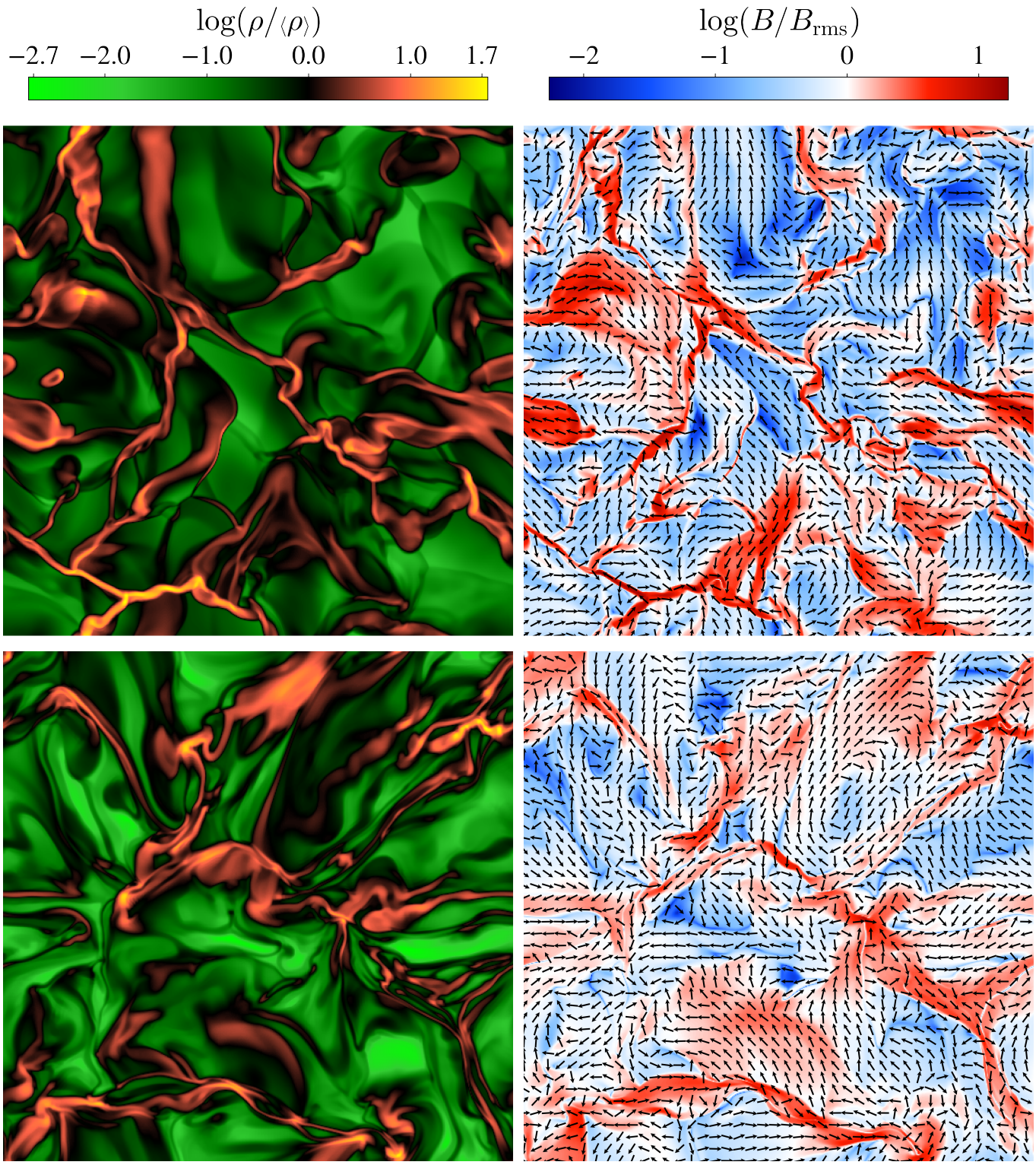

Figure 1. 2D slices in the $x-z$ plane at $y = 0.5$ from Pm1 (top row) and Pm10 (bottom row) in the saturated phase. The left panels show logarithmic density contrasts, $\log(\rho/\langle\rho\rangle)$, with the color scale ranging from low-density voids (green) to highly dense structures (red and yellow). The right panels display the logarithmic values of the normalized field strength, $\log(B/B_{\rm rms})$, with a blue-to-red color scale depicting regions of low-to-high field strengths. The arrows of equal length represent the directions of the in-plane magnetic field vectors.

field growth via random stretching. We find the weakening of the correlation to be more pronounced at high Pm. The steady-state values of r_p averaged over multiple independent realizations of the saturated state across different runs together with their 1σ variations are listed in Table 1. For Pm1, $\langle r_p\rangle$ is computed using eight realizations between $t/t_{\rm ed} = 46$ and 55 and 12 realizations each for both Pm5 and Pm10 covering $t/t_{\rm ed} = 32-46$ and $t/t_{\rm ed} = 32-45$, respectively. We find that while $\langle r_p\rangle$ attains values of $\approx$0.53 and $\approx$0.46 for Pm1 and Pm5, it declines steeply, settling to $\approx$0.34 for Pm10. Notably,

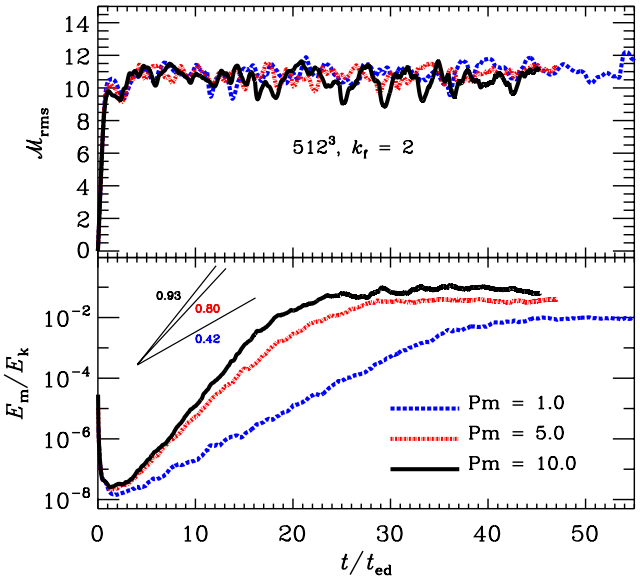

Figure 2. Evolution of $\mathcal{M}_{\rm rms}$ (top) and $E_{\rm m}/E_{\rm k}$ (bottom) with $t/t_{\rm ed}$ for Pm1 (blue dashed), Pm5 (red dotted), and Pm10 (black solid). While $\mathcal{M}_{\rm rms} \approx 11$ in the steady state, the growth rates in the kinematic phase and the saturation level of $E_{\rm m}/E_{\rm k}$ are strongly dependent on the Pm, with higher values producing faster exponential growth and higher saturation levels. The annotated slopes indicate the growth rates in the kinematic phases.

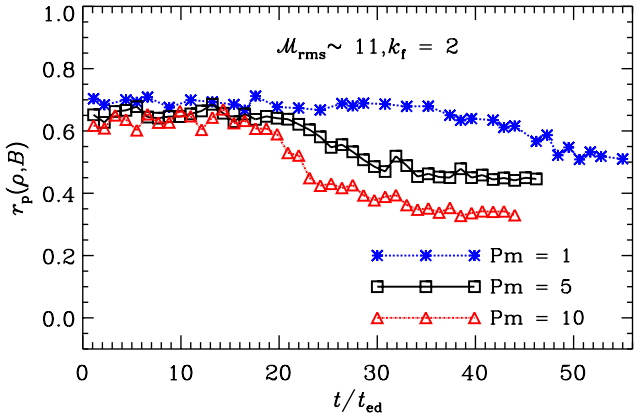

Figure 3. Evolution of the Pearson correlation coefficient $r_p(\rho, B)$ with $t/t_{\rm ed}$ for Pm1 (blue asterisks), Pm5 (black squares), and Pm10 (red triangles). Starting from a strong positive correlation, $r_p(\rho, B)$ drops as the dynamo evolves from the kinematic to saturated phase. The decrease in $r_p(\rho, B)$ is strongly dependent on Pm, with the Pm = 10 run decreasing by ≈52% from its value in the kinematic phase.

A. Seta & C. Federrath (2021b) obtained $\langle r_p \rangle \approx 0.56 \pm 0.02$ in their $\mathcal{M}_{\rm rms} \approx 10$, Pm = 1 simulation, which is very close to our Pm1 value.

The observed decrease in the degree of positive correlation in Pm10 likely highlights the role of magnetic pressure forces, as discussed in the Appendix. This interpretation is further supported by Figure 7, which shows the PDFs of the cosine of the angle between the unit vector of the gradient of the density ($\boldsymbol{n}_{\nabla\rho}$) and the gradient of magnetic pressure ($\boldsymbol{n}_{\nabla B^2}$). The figure clearly demonstrates that the antiparallel alignment between $\nabla\rho$ and ∇B^2 strengthens in the saturated phase for Pm > 1, while the parallel alignment weakens. This suggests that magnetic pressure forces oppose further compression of the field lines in the nonlinear saturated phase. As a result, density

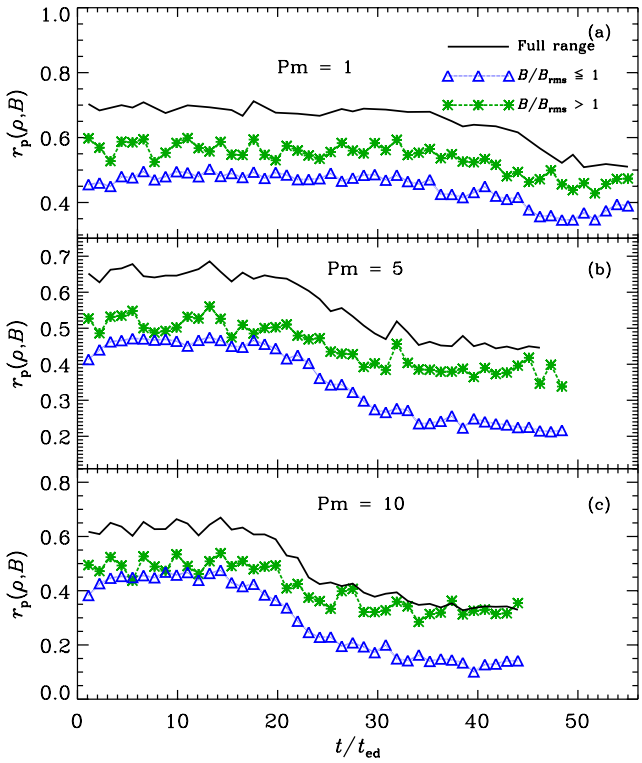

Figure 4. Evolution of $r_p(\rho, B)$ for Pm1 (top), Pm5 (middle), and Pm10 (bottom) in different ranges of $B/B_{\rm rms}$. The solid black line shows the evolution over the full range of magnetic field strengths similar to Figure 3. The blue open triangles represent $r_p(\rho, B)$ in regions where $B/B_{\rm rms} \leqslant 1$, while green asterisks denote correlations in regions with $B/B_{\rm rms} > 1$.

variations become more anticorrelated with variations in magnetic pressure at Pm > 1, leading to a steep decline in r_p.

4.1. Evolution of $r_p(\rho, B)$ in Regions of Strong/Weak Fields

To gain insight into the observed decrease of $r_p(\rho, B)$ with increasing Pm, we examine how this correlation evolves within regions of differing magnetic field strength, specifically, areas where $B/B_{\rm rms} \leqslant 1$ (weak fields) and $B/B_{\rm rms} > 1$ (strong fields). This analysis is presented in Figure 4, with panels (a), (b), and (c) corresponding to runs Pm1, Pm5, and Pm10, respectively. It is important to highlight that fluctuation dynamos naturally generate intermittent magnetic fields with a broad distribution of strengths, including regions with $B/B_{\rm rms} > 1$, even in incompressible turbulence, where amplification arises purely from random stretching. The supersonic regime studied here introduces an additional amplification due to compression that further broadens the high-B tail (S. Sur & K. Subramanian 2024). Thus, the strong field structures visible in Figure 1 arise from the combined effects of compression and random stretching, with compression enhancing but not uniquely producing the regions with $B/B_{\rm rms} > 1$.

In each panel, the solid black line depicts the evolution of $r_p(\rho, B)$ where no range of $B/B_{\rm rms}$ is considered. These lines correspond to those in Figure 3 and are presented here for an effective comparison. In the top panel, similar to the declining trend observed for the black solid curve, $r_p(\rho, B)$ also shows a declining trend in the strong field regime (green asterisks), although the correlation is consistently lower, fluctuating between 0.5 and 0.6 before settling to ≈0.45 in the saturated

state of the dynamo. For the weak field regime (blue triangles), the correlation is lower overall, starting around 0.5 and dropping steadily after $t/t_{\rm ed} \approx 30$, reaching a steady-state value of ≈0.36 by the end of the run. This suggests that at Pm = 1, ρ and B are moderately correlated, particularly in stronger field regions, but the correlation weakens over time, especially for weaker magnetic fields. In fact, even though r_p decreases by a similar factor in both strong and weak field regions, the overall higher value of r_p in the strong field regions implies that the compression of the fields due to density enhancements still dominates the ρ–B correlation.

For Pm = 5, panel (b) shows that strong field correlation (green asterisks) starts near 0.5 and decreases more gradually to a steady-state value of ≈0.39. In comparison, r_p for weak field regions (blue triangles) begins just below 0.5 but drops more steeply to values of ≈0.24. The rate of decline is more pronounced than in the Pm = 1 case, indicating stronger dissociation between ρ and B as the dynamo evolves to the saturated state. Finally, for Pm = 10, panel (c) shows that the trends continue with further reduction in $r_p(\rho, B)$. In this case, the strong field correlation (green asterisks) remains relatively higher than the weak field (blue triangles), with values fluctuating between 0.45 and 0.55 before settling to a steady-state value of ≈0.32. On the other hand, $r_p(\rho, B)$ in regions with $B/B_{\rm rms} \leqslant 1$ shows the most notable decline, starting at approximately 0.45 and reducing by a factor of ≈3 to settle at a steady-state value of ≈0.14. This reduction in r_p in the weak field regions is stronger compared to a decline by factor of ≈1.5 in the strong field regions.

In summary, a clear trend emerges across all three runs: as the Pm increases, the overall correlation between ρ and B decreases. The trend seen for Pm = 1 is similar to the findings in S. Sur & K. Subramanian (2024) for $\mathcal{M}_{\rm rms} = 3$. This decrease could be due to the fact that as magnetic fields grow in importance, forces due to magnetic pressure start to resist the further compression of field lines (S. Sur & K. Subramanian 2024). However, the Pm dependence of this decrease adds a new perspective to our results. In particular, the fact that the decrease in r_p is relatively minor in the strong field regions suggests that fields in those regions are constantly being amplified due to compressions in supersonic flows, which compensate for the magnetic pressure forces. On the other hand, the general sea of volume-filling $B/B_{\rm rms} \leqslant 1$ fields mainly arises due to random stretching. In the absence of strong compression in these regions, magnetic pressure forces manage to dominate over compression and reduce r_p. This effect is stronger at Pm = 10 compared to Pm = 1 due to efficient dynamo action in the former.

5. Power Spectra and Characteristic Scales

5.1. Power Spectra

Panels (a) and (b) in Figure 5 show the time evolution of the 1D shell integrated kinetic $K(k, t)$ and magnetic $M(k, t)$ spectra for runs Pm1 and Pm10, respectively. Here $K(k, t)$ is computed by weighting the velocity components by $\sqrt{\langle\rho\rangle}$. In both cases, we find that the slope of $K(k, t) \approx k^{-2.1}$, slightly steeper than the k^{-2} expected in hydrodynamic supersonic turbulence. The evolution of $M(k, t)$ is shown at different times from the kinematic to the saturated phase. In agreement with previous works (C. Federrath 2016; A. Seta & C. Federrath 2021a; S. Sur & K. Subramanian 2024), $M(k, t)$ evolves in a self-similar fashion that points to the nonlocal feature of the fluctuation dynamo in k-space (A. M. Shukurov & K. Subramanian 2021). In Pm1, we find that by $t/t_{\rm ed} = 55$, the magnetic energy is still less than the kinetic energy on all but very small scales beyond $k/k_{\rm min} \sim 40$.

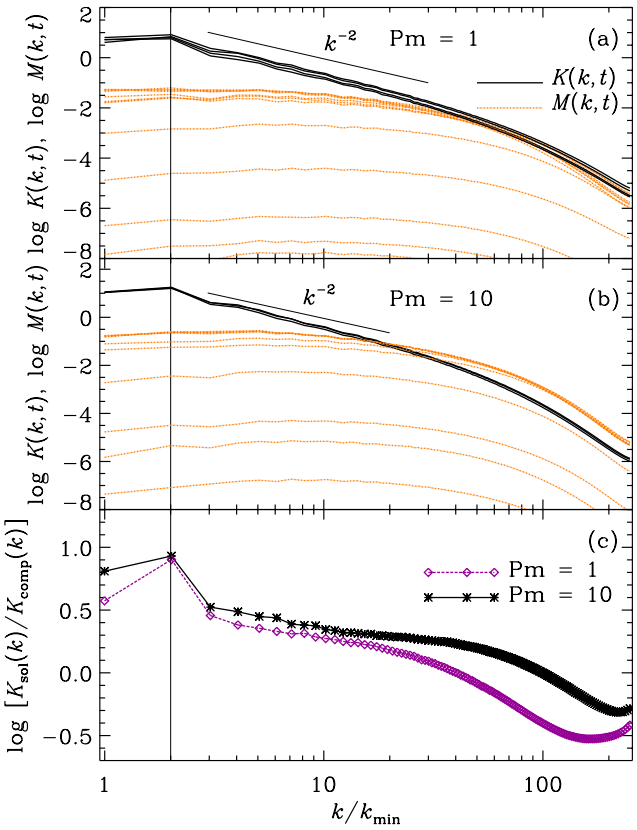

Figure 5. Kinetic $K(k, t)$ and magnetic $M(k, t)$ energy spectra for Pm1 and Pm10 at fixed Rm. Panels (a) and (b) show the time evolution of $K(k, t)$ (solid black lines) and $M(k, t)$ (dotted orange lines) as functions of wavenumber $k/k_{\rm min}$ for Pm = 1 and Pm = 10, respectively. Panel (c) shows the time-averaged ratio of solenoidal to compressive components of the kinetic energy spectrum, $K_{\rm sol}(k)/K_{\rm comp}(k)$, for both runs in the saturated phase of the dynamo. Higher Pm leads to a relatively larger solenoidal energy fraction at intermediate and small scales and enhances magnetic energy at small scales compared to the Pm = 1 case. The thin vertical line at $k/k_{\rm min} = 2$ is the turbulence driving scale, where $k_{\rm min} = 2\pi\, L^{-1}$ is the smallest wavenumber in the box. The $K(k, t)$ shown here are density-weighted velocity spectra ($\sqrt{\langle\rho\rangle}\,\boldsymbol{U}$). Since $\langle\rho\rangle \approx 1$ in our simulation volume, the weighting does not affect the spectral slopes.

The bottom panel in Figure 5 shows the time-averaged spectra of the ratio of solenoidal to compressive kinetic energy, $K_{\rm sol}(k)/K_{\rm comp}(k)$, for Pm1 (dashed, diamonds) and Pm10 (solid, asterisks) in the saturated phase. This is obtained by first decomposing the velocity field into divergence-free ($\boldsymbol{U}_{\rm sol}$) and curl-free ($\boldsymbol{U}_{\rm comp}$) components using a Hodge–Helmholtz decomposition, followed by evaluating the spectra of $K_{\rm sol}(k)$ and $K_{\rm comp}(k)$. Recall that in our simulations, the Rm is held fixed, so increasing Pm implies increasing ν while keeping η constant. This choice isolates the effects of viscous dissipation on the velocity field, which in turn affects the solenoidal and compressive components differently.

For example, at high Pm (e.g., Pm10), the viscosity is large, which selectively damps out small-scale velocity fluctuations —but crucially, this damping is stronger for compressive motions, which involve velocity divergence and hence strong density and pressure gradients. On the other hand, solenoidal

Table 2
Time-averaged Values and 1σ Variations of the Ratio of Different Characteristic Scales in the Saturated Phase

Run	Pm	$\langle \ell_{\rm int}^V/\ell_{\rm int}^M\rangle_{\rm sat}$	$\langle \ell_\nu/\ell_\eta\rangle_{\rm sat}$
Pm1	1	3.40 ± 0.20	1.36 ± 0.05
Pm5	5	3.43 ± 0.18	1.70 ± 0.03
Pm10	10	3.40 ± 0.15	1.92 ± 0.05

motions, being divergence-free, do not generate such gradients and are more resilient against viscous damping. As a result, in Pm10, compressive motions are preferentially suppressed at small-to-intermediate scales, leading to a higher solenoidal-to-compressive energy ratio over much of the inertial and dissipation ranges. Thus, the black solid curve (Pm = 10) lies well above the purple dotted curve (Pm = 1) across a wide range of k.

In contrast, for Pm1, viscosity and resistivity are the same. The flow experiences less viscous damping overall, and compressive motions can survive and even thrive in the highly supersonic regime (with $\mathcal{M}_{\rm rms} \approx 11$). Shocks and compressive features are naturally produced in such flows, and when not heavily damped by viscosity, they maintain a significant fraction of the kinetic energy budget. Hence, the solenoidal-to-compressive energy ratio is lower for Pm1, as seen in the purple curve.[6]

5.2. Characteristic Scales from Power Spectra

Using the energy spectra $K(k, t)$ and $M(k, t)$, we first estimate the integral scales of the velocity and magnetic fields, defined as

$$\ell_{\rm int}^V = \frac{2\pi \int [K(k,t)/k]\, dk}{\int K(k,t)\, dk}, \qquad \ell_{\rm int}^M = \frac{2\pi \int [M(k,t)/k]\, dk}{\int M(k,t)\, dk}. \tag{6}$$

Across all runs (Pm1, Pm5, and Pm10), we find that $\ell_{\rm int}^V$ remains nearly constant as the dynamo evolves, whereas $\ell_{\rm int}^M$ grows by a factor of $\sim$2 from the kinematic to the saturated phase. This is due to the influence of Lorentz forces that leads to a larger coherence scale of the magnetic field. The third column of Table 2 lists the time-averaged ratio of $\ell_{\rm int}^V/\ell_{\rm int}^M$ in the saturated phase, using nine realizations for Pm1 and 12 realizations each for the Pm5 and Pm10 runs. In all cases, $\ell_{\rm int}^V$ exceeds $\ell_{\rm int}^M$ by a factor of $\sim$3.4, implying that even after saturation, most magnetic energy remains at $k > k_{\rm f}$. The independence of this ratio on Pm likely arises from fixing Rm while reducing Re to realize Pm > 1.

We now turn to evaluating the viscous and resistive dissipation scales of the velocity and magnetic fields from the spectra $K(k, t)$ and $M(k, t)$. Commonly, the characteristic dissipation wavenumbers of the velocity fields are computed from the maximum of the dissipation spectra, $k_\nu = \left[\int k^2 K(k)\, dk / \int K(k)\, dk\right]^{1/2}$ (and analogously for magnetic dissipation). However, this approach may be unreliable, as the location of the peak can be highly sensitive to the localized spectral features. Hence, to obtain a more robust measure, we define the viscous and resistive dissipation wavenumbers as

$$k_\nu = \frac{\int k\, [k^2\, K(k,t)]\, dk}{\int k^2\, K(k,t)\, dk}, \qquad k_\eta = \frac{\int k\, [k^2\, M(k,t)]\, dk}{\int k^2\, M(k,t)\, dk}, \tag{7}$$

which accounts for the contribution from the full dissipation spectrum and therefore provides a more reliable estimate of the dissipation scales. The resulting ratio of the dissipation length scales $\ell_\nu/\ell_\eta = k_\eta/k_\nu$.

The time-averaged ratio $\langle \ell_\nu/\ell_\eta\rangle$ in the saturated phase of the dynamo is shown in the last column in Table 2, computed over the same number of independent realizations as done for the ratio of integral scales. For Pm = 1, we obtain $\langle \ell_\nu/\ell_\eta\rangle \sim 1.36$. At higher Pm, the ratios increase to $\sim$2 at Pm = 10. Our results thus preserve the trend that the separation between ℓ_ν and ℓ_η widens as Pm increases.

6. Stretching versus Compression

Magnetic field amplification via dynamo action in supersonic turbulence results from a complex interplay of random stretching and compression of magnetic field lines. Understanding how these two processes compete and whether their relative influence depends on the magnetic Prandtl number (Pm) is one of the key objectives of our work. To investigate this, we examine the PDFs of local stretching and compression that contribute to the growth or decay of magnetic energy.

Following S. Sur & K. Subramanian (2024), the evolution equation of the magnetic energy in terms of local stretching, advection, compression, and dissipation terms is

$$\frac{\partial}{\partial t}\left(\frac{B^2}{2}\right) = \underbrace{B_i B_j \frac{\partial U_i}{\partial x_j}}_{\text{stretching}} - \underbrace{B_i \frac{\partial U_j}{\partial x_j} B_i}_{\text{compression}} - \underbrace{B_i U_j \frac{\partial B_i}{\partial x_j}}_{\text{advection}} - \underbrace{\eta B_i (\nabla \times \boldsymbol{J})_i}_{\text{dissipation}}. \tag{8}$$

The velocity gradient $\partial U_i/\partial x_j$ in the above equation can be further decomposed as a sum of three terms: a rate of strain tensor,

$$S_{ij} = (\partial U_i/\partial x_j + \partial U_j/\partial x_i)/2 - (\partial_k U_k)\delta_{ij}/3; \tag{9}$$

a rate of expansion tensor, $(\partial_k U_k)\delta_{ij}/3$; and an antisymmetric tensor,

$$\Omega_{ij} = \epsilon_{ijk}\omega_k/2, \tag{10}$$

corresponding to the vorticity. It is straightforward to show that the antisymmetric part does not contribute to the magnetic energy, as it is proportional to $\boldsymbol{B} \cdot (\boldsymbol{B} \times \omega) = 0$. Substituting Equations (9) and (10) in (8), we get

$$\frac{\partial}{\partial t}\left(\frac{B^2}{2}\right) = \underbrace{B_i B_j S_{ij}}_{\text{stretching}} + \underbrace{\frac{1}{3} B_i B_j \delta_{ij} (\partial_k U_k)}_{\text{expansion}} - \underbrace{B_i \frac{\partial U_j}{\partial x_j} B_i}_{\text{compression}} - \underbrace{B_i U_j \frac{\partial B_i}{\partial x_j}}_{\text{advection}} - \underbrace{\eta B_i (\nabla \times \boldsymbol{J})_i}_{\text{dissipation}}. \tag{11}$$

It is worth noting that the presence of $(\partial_k U_k)$ in S_{ij} implies that local stretching is also influenced by flow compressibility. For incompressible flows, this effect is negligible. The expansion and compression terms in Equation (11) combine

[6] The rise of $K_{\rm sol}(k)/K_{\rm comp}(k)$ at $k/k_{\rm min} > 100$ reflects resolution-dependent numerical artifacts confined to the dissipation range and does not affect the inertial-range results.

Table 3
Time-averaged Values of ξ_s and ξ_c Obtained from the PDFs of Stretching and Compression Terms in Equation (12) in the Kinematic and Saturated Phases

Run	Pm	ξ_s		ξ_c	
		Kin.	Sat.	Kin.	Sat.
Pm1	1	7.07 ± 0.31	2.33 ± 0.15	8.35 ± 0.23	1.77 ± 0.13
Pm5	5	4.57 ± 0.21	2.22 ± 0.07	4.48 ± 0.18	1.40 ± 0.12
Pm10	10	3.59 ± 0.16	1.62 ± 0.11	2.85 ± 0.21	0.56 ± 0.10

into a term $\propto \nabla \cdot \boldsymbol{U}$, while the advection term can be rewritten as $U_j \partial_j (B_i^2/2)$. Multiplying both sides of Equation (11) by $t_{\rm ed}/B_{\rm rms}^2$, we obtain the volume-integrated magnetic energy evolution in dimensionless form,

$$\int_V \frac{\partial}{\partial t}\left(\frac{|\boldsymbol{B}|^2}{2}\right)\frac{t_{\rm ed}}{B_{\rm rms}^2}\,dV = +\int_V S_{ij}B_iB_j\frac{t_{\rm ed}}{B_{\rm rms}^2}\,dV - \frac{2}{3}\int_V |\boldsymbol{B}|^2(\nabla\cdot\boldsymbol{U})\frac{t_{\rm ed}}{B_{\rm rms}^2}\,dV - \int_V \boldsymbol{U}\cdot\frac{1}{2}\nabla|\boldsymbol{B}|^2\frac{t_{\rm ed}}{B_{\rm rms}^2}\,dV - \eta\int_V \boldsymbol{B}\cdot(\nabla\times\boldsymbol{J})\frac{t_{\rm ed}}{B_{\rm rms}^2}\,dV. \quad (12)$$

Following the approach described in S. Sur & K. Subramanian (2024), we compute the PDFs for the dimensionless stretching and compression terms in Equation (12) and derive the corresponding mean values, ξ_s (stretching) and ξ_c (compression). Table 3 lists these means averaged over several independent realizations of the dynamo (at different $t_{\rm ed}$) in the kinematic and saturated phases.

In line with the expectation that both stretching and compression are influenced by flow compressibility, our analysis across all three simulations reveals a consistent decrease in both ξ_s (stretching) and ξ_c (compression) as the dynamo transitions from the kinematic to the nonlinear saturated phase. Interestingly, and in contrast to the expectation that line stretching should dominate over compression, Pm1 shows that magnetic energy growth during the kinematic phase is actually driven primarily by compression, with stretching remaining subdominant by a factor of $\approx$1.2. This is because both viscous and resistive dissipation act on comparable scales such that the shocks remain effective in driving density compressions that amplify the fields. However, as the dynamo evolves into the saturated phase, both mechanisms are suppressed. The suppression is significantly stronger for compression, with ξ_c decreasing by a factor of $\approx$4.7 compared to a decrease by a factor of about 3 for ξ_s.

In Pm5, stretching and compression are initially comparable ($\xi_s \approx \xi_c$) in the kinematic phase, but compression again declines more sharply in the saturated regime. For Pm10, the behavior shifts. Here, line stretching clearly dominates over compression in the kinematic phase, by a factor of about 1.26. This is due to the fact that a higher viscosity suppresses velocity fluctuations on scales larger than the resistive scales. This suppression reduces the compressive motions that are more easily dissipated by viscosity. As a result, line stretching from vortical motions becomes the dominant agent in amplifying the field. Notably, in the saturated phase, compression is suppressed even more dramatically with ξ_c dropping by a factor of $\sim$5 compared to its kinematic value—greater than the suppression seen for Pm = 1 and 5. In all three runs, the stronger suppression of compressive motions relative to stretching once again reinforces the role of magnetic pressure forces in resisting further compression (S. Sur & K. Subramanian 2024).

7. Faraday Rotation from $3N^2$ Lines of Sight

Faraday rotation serves as a key probe of the line-of-sight (LOS) component of magnetic fields in astrophysical plasmas. In a magnetized environment such as the galactic ISM, the polarization angle of linearly polarized radio emission undergoes a wavelength-dependent rotation. The angle of rotation increases with the square of the wavelength, and the proportionality factor is known as RM,

$$\mathrm{RM} = K\int_L n_{\rm e}\,\boldsymbol{B}\cdot d\boldsymbol{\ell}, \quad (13)$$

where $n_{\rm e}$ is the thermal electron density, $\boldsymbol{B}$ is the magnetic field vector, and the integration is along the LOS L from the source to the observer. The constant $K = 0.81\,\mathrm{rad\,m^{-2}\,cm^3\,\mu G^{-1}\,pc^{-1}}$ encapsulates physical constants. In what follows, we explore how coherent the fields generated by fluctuation dynamos in supersonic turbulence are and assess how this coherence varies with Pm. Since supersonic flows result in significant density fluctuations along the LOS, we retain $n_{\rm e}$ inside the integral for all the runs. Following the methodology outlined in S. Sur et al. (2018), we compute $\int \rho\boldsymbol{B}\cdot d\boldsymbol{l}$ directly for each simulation listed in Table 1, evaluating the RM over $3N^2$ LOSs, along each of the x-, y-, and z-directions. For example, if the LOS integration is along z, the RM at a transverse position (x_i, y_i) is given by the discrete sum of B_z,

$$\mathrm{RM}(x_i, y_i, t) = \frac{K}{\mu m_p}\sum_{j=0}^{N-1}\left(\frac{L}{N}\right)\rho B_z\left(x_i, y_i, \frac{L}{N}j, t\right), \quad (14)$$

>where $n_{\rm e} = \rho/\mu m_p$ is expressed in terms of the density, L is the box length, N is the number of grid points along each axis, $\mu = 0.61$ is the mean molecular weight, and m_p is the proton mass. Because our simulations are isothermal, the gas temperature is fixed and the ionization fraction is implicitly constant. Thus, the thermal electron density scales linearly with the gas density ($n_{\rm e} \propto \rho$), resulting in a perfect point–point correlation. In a realistic ISM, however, this correlation can vary substantially as radiative cooling and recombination lower the ionization fraction in dense, cold gas, leading to a corresponding reduction in $n_{\rm e}$ (e.g., A. Bracco et al. 2022). However, the dominant contribution to the observable RM typically arises from the warm ionized medium (WIM) and other diffuse ionized phases (M. Haverkorn 2015; A. Seta & C. Federrath 2022), where the electron fraction is relatively high and hence the assumption of a local proportionality between $n_{\rm e}$ and ρ remains a reasonable approximation. In this sense, the RM analysis presented here applies to an idealized, WIM-like medium. This provides a clean and unambiguous framework for quantifying the magnetic coherence scale produced by the fluctuation dynamo in highly compressible

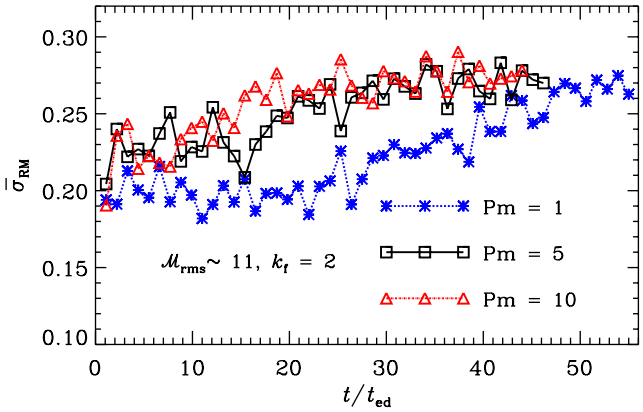

Figure 6. Time evolution of $\bar{\sigma}_{RM}$ with t/t_{ed} for all runs listed in Table 1.

turbulence, without the additional complications introduced by a multiphase ISM.

Magnetic fields generated by the fluctuation dynamo are expected to be nearly statistically isotropic, leading to a vanishing mean RM, i.e., $\langle \int \rho \boldsymbol{B} \cdot d\boldsymbol{l} \rangle = 0$. We thus concentrate on the standard deviation of the RM, σ_{RM}, and examine its time evolution across different values of Pm. To facilitate comparisons across different runs and physical regimes, we further normalize σ_{RM} by a characteristic value,

$$\sigma_{RM0} = \frac{K}{\mu m_p} \frac{(\rho B)_{rms}}{\sqrt{3}} L \sqrt{\frac{2\pi}{k_f L}}, \tag{15}$$

assuming that magnetic fields (weighted by density) are randomly oriented within turbulent cells of correlation length $l_f = 2\pi/k_f$ in a box of size L. This assumption is justified for supersonic flows, where density fluctuations could significantly vary from one turbulent cell to another and can also be correlated with magnetic field variations. Using the above normalization, we next compute the evolution of the normalized standard deviation $\bar{\sigma}_{RM} = \sigma_{RM}/\sigma_{RM0}$ of the set RM(x_i, y_i, t). For LOSs along x and y, B_x and B_y values are to be used, respectively, in Equation (14). The final $\bar{\sigma}_{RM}$ value is obtained by averaging the standard deviations computed along the three principal directions. For reference, a fluctuation-dynamo-generated field ordered on the forcing scale would have $\bar{\sigma}_{RM} \sim 1$.

Figure 6 illustrates the temporal evolution of $\bar{\sigma}_{RM}$ for the three runs, differing in Pm values. Overall, in each simulation, $\bar{\sigma}_{RM}$ starts from a value of 0.2 and then increases as the fluctuation dynamo starts to amplify the field. As $\bar{\sigma}_{RM}$ rises above ∼0.22, subtle differences between the runs emerge. For Pm1 (blue asterisks), $\bar{\sigma}_{RM}$ continues to fluctuate around ∼0.2 until $t/t_{ed} \approx 23$, after which it increases slowly until $t/t_{ed} \approx 46$. Even though the magnetic energy saturates by $t/t_{ed} \approx 40$ (see Figure 2), the slow increase of $\bar{\sigma}_{RM}$ reflects the fact that Lorentz forces continue to reorganize the field, which may modestly increase the magnetic coherence scale. This structural adjustment naturally produces a residual evolution in $\bar{\sigma}_{RM}$ up to $t/t_{ed} \approx 46$. Additionally, since $\bar{\sigma}_{RM}$ is an integral quantity, it is sensitive to intermittency and variations in (ρ−B) correlations across many sight lines. Therefore, snapshot-to-snapshot variations are expected and indeed seen in each of the three curves in the figure. On the other hand, efficient dynamo action in the Pm > 1 runs leads to a gradual increase in $\bar{\sigma}_{RM}$ for Pm5 (black squares) and Pm10 (red triangles), noticeable after $t/t_{ed} \approx 10$. This early increase in $\bar{\sigma}_{RM}$ could be attributed to the fact that at Pm > 1, eddies richer in vorticity are less impeded by viscosity. Beyond $t/t_{ed} \approx 20$, the curves for Pm = 5 and 10 settle into a quasi-steady state, while the curve for Pm = 1 keeps evolving and only reaches a steady state at $t/t_{ed} \approx 44$. Despite the difference in evolution, we find that the time-averaged $\langle \bar{\sigma}_{RM} \rangle \approx 0.26 \pm 0.005$ for Pm1, ≈0.26 ± 0.01 for Pm5, and ≈0.27 ± 0.009 for Pm10. These values are computed using nine realizations for Pm1 and 17 realizations each for Pm5 and Pm10 over the intervals $t/t_{ed} = 47-55$, 25−46, and 25−45, respectively. This implies that the steady-state value of $\bar{\sigma}_{RM}$ is nearly independent of Pm once the dynamo saturates but is lower for Pm = 1 in the kinematic phase. The similarity in the steady-state values of $\langle \bar{\sigma}_{RM} \rangle$ across all the runs imply that the effect of the Lorentz forces is to order the field on a maximum scale that depends only on the forcing scale. In our simulations, this Lorentz-force-regulated magnetic coherence scale saturates at ≈(1/4−1/3)ℓ_f, when the driving scale is at half the scale of the simulation domain.

8. Conclusions

Fluctuation dynamos provide a key mechanism for amplification of seed magnetic fields in random/turbulent flows by the action of turbulent eddies. In the ISM, which is both highly conducting and compressible, these dynamos operate by a combination of random (in time) stretching and compression of magnetic field lines (e.g., C. Federrath et al. 2011a; C. Federrath 2016; A. Seta & C. Federrath 2021a; S. Sur & K. Subramanian 2024). In this work, we have carried out a systematic study of fluctuation dynamos in supersonic turbulence ($\mathcal{M}_{rms} \approx 11$), investigating their dependence on the magnetic Prandtl number up to Pm = 10. In what follows, we delineate the important findings from our work with an emphasis on the distinct characteristics obtained between the Pm = 1 and Pm > 1 regimes.

The time evolution of E_m/E_k shows a clear dependence on Pm, with larger Pm yielding faster growth rates and higher saturation levels than Pm = 1. The 2D slices of $\log(\rho/\langle\rho\rangle)$ display the characteristic features of supersonic turbulence, namely, sharp density contrasts where dense structures are surrounded by underdense voids. We also find the in-plane magnetic fields to be arranged in folds and strongly compressed at myriad locations indicating field amplification by a combination of local stretching and compression. Differences between the Pm = 1 and Pm > 1 regimes also emerge in the time evolution of the Pearson correlation coefficient "r_p" of the density and magnetic field strength. Specifically, during the transition from the kinematic to the nonlinear saturated phase, r_p decreases only by a factor of 1.2 for Pm = 1 but by ∼2 for Pm = 10. This stronger suppression for Pm = 10 reflects the role of magnetic pressure forces in resisting the continued compression of the field lines due to supersonic turbulence. In fact, as Figure 7 clearly illustrates, the antiparallel alignment between $\nabla\rho$ and ∇B^2 is more pronounced for Pm = 10 than for Pm = 1. Moreover, separating regions by field strength reveals that the enhanced suppression of r_p for Pm = 10 arises mainly from the reduced correlation between ρ and B in sub-rms ($B/B_{rms} \leqslant 1$) regions, although the correlation also weakens in the strong field ($B/B_{rms} > 1$) regime.

Analysis of the solenoidal and compressive kinetic energy spectra shows that, for Pm = 10, higher viscosity suppresses small-scale velocity fluctuations more strongly in compressive than in solenoidal modes. Consequently, the solenoidal-to-compressive kinetic energy ratio is larger than in the Pm = 1 case. Estimates of the integral scales of the velocity and magnetic fields in the saturated phase show that the ratio of $\ell_{\rm int}^V/\ell_{\rm int}^M$ is independent of Pm, yielding values of ∼3.4. This suggests that even in the nonlinear phase, the magnetic energy remains peaked on scales $k > k_{\rm f}$. On the other hand, our numerical estimates of the viscous-to-resistive dissipation scale ratio exhibit an increase with Pm, with $\langle \ell_\nu/\ell_\eta \rangle \approx 1.36$ for Pm = 1, ≈1.70 for Pm = 5, and ≈1.92 for Pm = 10. This monotonic behavior is consistent with the expectation that higher Pm yields a broader separation between viscous and resistive scales.

Comparison of the contributions from line stretching and compression reveals key differences between Pm = 1 and Pm > 1. Note that in incompressible flows, the decline in $\xi_{\rm s}$ during the nonlinear phase reflects reduced stretching (S. Sur & K. Subramanian 2024). In compressible flows, however, both stretching and compression are modified by density fluctuations. For Pm = 1, we find $\xi_{\rm c} > \xi_{\rm s}$ in the kinematic phase, indicating that field amplification is initially driven by compression associated with density enhancements. As the system saturates, both $\xi_{\rm s}$ and $\xi_{\rm c}$ decrease, with stronger suppression of $\xi_{\rm c}$. For Pm = 5, $\xi_{\rm s} \approx \xi_{\rm c}$ in the kinematic phase, but stretching again dominates in the saturated phase. However, for Pm = 10, amplification in the kinematic phase is initially driven by random stretching rather than compression, likely due to the higher viscosity (Re ≈ 660), which hinders flux tube compression. In the saturated phase, both terms decrease, but $\xi_{\rm c}$ is suppressed by nearly a factor of 5. Irrespective of the Pm, the stronger suppression of $\xi_{\rm c}$ in the saturated phase reflects the role of magnetic pressure opposing further compression in agreement with S. Sur & K. Subramanian (2024).

In summary, the aforementioned results in the saturated phase show the following trends: (i) $\langle r_p \rangle$ decreases with increasing Pm; (ii) $\langle \ell_{\rm int}^V/\ell_{\rm int}^M \rangle$ remains constant across Pm, while $\langle \ell_\nu/\ell_\eta \rangle$ increases with Pm; and (iii) the PDFs of the stretching and compression terms reveal that in the kinematic phase, compression dominates for Pm1, both terms are comparable for Pm5, and stretching dominates for Pm10. In all three runs, stretching dominates over compression in the saturated phase. To assess the statistical significance of these results, we use the mean (μ) and the 1σ scatter of the relevant variables together with the number of realizations "N" to compute the standard error of the mean, SEM = $\sigma/\sqrt{N}$. Differences between runs are then evaluated via pairwise comparisons of the mean values, taking into account the combined SEMs of each pair of runs[7] (P. R. Bevington & D. K. Robinson 2003; J. V. Wall & C. R. Jenkins 2012).

The SEMs of $\langle r_p \rangle$ for Pm1, Pm5, and Pm10 are 7×10^{-3}, 3×10^{-3}, and 2.89×10^{-3}, respectively. The pairwise differences (0.08–0.19) exceed the combined SEMs by factors of (10–25), confirming that the decline in $\langle r_p \rangle$ with increasing Pm is statistically significant. In contrast, pairwise differences for $\langle \ell_{\rm int}^V/\ell_{\rm int}^M \rangle$ are ⩽0.03, smaller than the corresponding SEMs, consistent with the lack of significant Pm dependence. Conversely, for $\langle \ell_\nu/\ell_\eta \rangle$, the mean differences (0.22−0.56) are 1–2 orders of magnitude larger than the SEMs, indicating that the increase in $\langle \ell_\nu/\ell_\eta \rangle$ with Pm is statistically robust. Similar analyses for the stretching and compression terms show that at Pm1, the strong compression dominance in the kinematic phase is confirmed by the pairwise difference being ∼12 times larger than the combined SEM. For Pm5, stretching and compression become statistically indistinguishable, with the difference only ∼1.2 times the combined SEM, indicating a transitional regime where neither mechanism dominates. At Pm10, stretching already dominates in the kinematic phase, with the difference exceeding the combined SEM by a factor of ∼10. In all three runs, the saturated phase shows a robust dominance of stretching over compression, with differences (8−25) times larger than the combined SEMs, reflecting the suppression of compressive amplification once the Lorentz force becomes dynamically important.

Finally, we examined the coherence of fluctuation-dynamo-generated fields in supersonic turbulence ($\mathcal{M}_{\rm rms} \approx 11$). Results from our synthetic RM measurements for Pm = 1−10 yield coherence scales $\ell_{\rm c} \sim (1/4-1/3)\ell_{\rm f}$ for driving at half the box scale. Using the mean and 1σ values from Section 7 and $N = 9$, 17, and 17, we obtain SEMs $(1.6 \times 10^{-3}, 2.4 \times 10^{-3}, 2.1 \times 10^{-3})$ for Pm1, Pm5, and Pm10, respectively. Analysis of the difference between the means suggests that while Pm1 and Pm5 are statistically indistinguishable, Pm10 shows only a very small difference (∼3.6%). This confirms that within the range of Pm values explored in this work, $\bar{\sigma}_{\rm RM}$ is nearly independent of Pm.

In recent years, Mg II absorption systems studied by M. L. Bernet et al. (2008, 2010), J. S. Farnes et al. (2014), and S. Malik et al. (2020) have revealed excess Faraday rotation consistent with ordered magnetic fields of μG strength in galaxies out to $z \sim 1$, when the Universe was only 6 billion yr old. This motivates assessing whether fluctuation dynamos in compressible turbulence can account for a significant component of the RM signal.

For a physical estimate, we note that the total stellar mass of the Milky Way is $\sim 2.6 \times 10^{10}\, M_\odot$ (J. Lian et al. 2025), with a gas mass fraction assumed to be of order 10%. Assuming that this gas is distributed in a disk of radius $r = 10$ kpc and thickness $2h = 1$ kpc, the average number density $n \sim 0.4\,{\rm cm}^{-3}$. It is plausible that high-redshift star-forming disks may exhibit substantially larger gas fractions, so the corresponding electron densities may exceed those typical of the Milky Way WIM. Indeed, nebular diagnostics of [S II] and [O II] doublets in $z \sim 1-2$ galaxies yield internal H II region electron densities, $n_{\rm e} \approx (50-300)\,{\rm cm}^{-3}$ (M. Kaasinen et al. 2017; R. L. Davies et al. 2021). If such ionized clumps have modest filling factors $f_V \sim 0.01-0.1$, the resulting $\bar{n}_{\rm e} \sim (0.5 - 30)\,{\rm cm}^{-3}$. For simplicity, and to remain conservative, we adopt $\bar{n}_{\rm e} \sim 1\,{\rm cm}^{-3}$.

Assuming typical vortical turbulent velocities of $u_{\rm rms} \sim 10\,{\rm km\,s}^{-1}$ of the order of the sound speed in the WIM and a forcing scale of $\ell_{\rm f} \sim 100$ pc, the eddy turnover time is $t_{\rm ed} \sim 10^7$ yr, enabling the fluctuation dynamo to grow and saturate the fields well within the lifetime of disk galaxies. For a path length of $L = 1$ kpc through the disk thickness, the

[7] For two runs A and B with means μ_A and μ_B, the pairwise difference is $\Delta = |\mu_A - \mu_B|$, and the combined SEM is ${\rm SEM}_c = \sqrt{{\rm SEM}_A^2 + {\rm SEM}_B^2}$.

normalization factor is

$$\sigma_{\rm RM0} \sim 444 \ \ {\rm rad\ m^{-2}} \left(\frac{\bar{n}_{\rm e}}{1\ {\rm cm^{-3}}}\right) \times \left(\frac{B_{\rm rms}}{3\ \mu{\rm G}}\right)\left(\frac{L}{1\ {\rm kpc}}\right)^{1/2}\left(\frac{l_{\rm f}}{100\ {\rm pc}}\right)^{1/2}, \quad (16)$$

obtained from a simple model of random magnetic fields, where the fields are assumed to be random with a correlation length $\ell_{\rm f} = 2\pi/k_{\rm f}$ (e.g., D. Sokoloff et al. 1998; K. Subramanian et al. 2006; J. Cho & D. Ryu 2009; P. Bhat & K. Subramanian 2013; S. Sur et al. 2018; A. Seta & C. Federrath 2021b). The equipartition field $B_{\rm eq} = (4\pi\ \rho\ u_{\rm rms}^2)^{1/2} \sim 5\ \mu$G. If the fluctuation dynamo saturates at a fraction $f \sim (0.1-0.2)$ of equipartition, we obtain $B_{\rm rms} = fB_{\rm eq} \approx (0.5-1)\ \mu$G,[8] giving $\sigma_{\rm RM0} \sim (74-150)\ {\rm rad\ m^{-2}}$. Thus, for $\bar{\sigma}_{\rm RM} \sim 0.3$, the Faraday RM dispersion is $\sim$(22–45) rad m^{-2}. This level of RM dispersion is comparable to the RM excess values reported for Mg II absorbers, which range from tens of rad m^{-2} (J. S. Farnes et al. 2014) to $\geqslant$100 rad m^{-2} for strong absorbers (M. L. Bernet et al. 2008). This suggests that fluctuation dynamos in gas-rich, turbulent disks at $z \sim 1$ could plausibly account for a substantial fraction of the observed RM signal. However, several caveats apply: (i) our estimates assume a uniform disk geometry rather than clumpy circumgalactic medium/ISM structures; (ii) the true filling factors, thermal electron densities, efficiency of the dynamo, and turbulent driving scales in high-z galaxies are uncertain; and (iii) Mg II absorbers may probe both disk and halo gas, whereas our estimates pertain strictly to disklike environments. In addition, observed extragalactic RMs include contributions from the Galactic foreground, intrinsic source rotation, and redshift-dependent depolarization, all of which introduce systematic uncertainties when attributing the RM signal to intervening galaxies. In this context, our estimates of RM dispersions that are broadly comparable to observationally inferred RM excesses offer a useful theoretical framework for their interpretation.

We further emphasize that in supersonic turbulence, the use of a volume-averaged $\bar{n}_{\rm e}$ in estimating $\sigma_{\rm RM0}$ is an approximation, valid primarily for order-of-magnitude comparisons. In practice and as shown earlier, density fluctuations can be significant and correlated with magnetic field variations. Our simulation-based RM values retain the full spatial variation of ρ within the LOS integrals to capture these effects accurately.

In a realistic ISM, the ionized phases typically occupy only a fraction $f_V < 1$ of the total volume. Let us consider an LOS of total length L that passes through N turbulent cells of size $\ell_{\rm f}$. If only a fraction f_V of the LOS is filled with the ionized gas, then $N = f_V L/\ell_{\rm f}$, instead of $N = L/\ell_{\rm f}$ for $f_V = 1$. Consequently, $\sigma_{\rm RM} \propto f_V^{1/2}$, whereas the normalized quantity $\bar{\sigma}_{\rm RM}$ is independent of f_V. Thus, although the absolute RM dispersion decreases by $f_V^{1/2}$, the normalized RM statistics reported in our work remain representative of the intrinsic magnetic coherence properties.

Given that the ISM is inherently multiphase, a natural next step is to extend this work to more realistic simulations that include cooling, heating, and phase structure. Such studies would clarify how spatially varying Pm and different driving mechanisms shape the fluctuation dynamo and how these effects propagate into the resulting magnetic field topology and Faraday RMs.

[8] The magnetic field in clouds denser than the average ISM could be larger than the $B_{\rm rms}$ estimated above.

Acknowledgments

A.N. and S.S. acknowledge the use of the High Performance Computing resources made available by the Computer Centre of IIA. S.S. and B.V. thank Mr. Sayeed Kazim H. for testing an earlier version of the turbulence driving module as part of his MSc thesis project at IIT Indore. The authors thank Prof. Andrea Mignone for valuable discussions and the reviewer for a timely and constructive report.

Software: Astropy (A. M. Price-Whelan et al. 2018), h5py (Collette 2013), Jupyter (T. Kluyver et al. 2016), Matplotlib (J. D. Hunter 2007), Numpy (C. R. Harris et al. 2020), Scipy (P. Virtanen et al. 2020).

Appendix
Alignment Angles

In Figure 7, we present the PDFs of the cosine of the angle between the gradient of the density and the gradient of magnetic pressure for Pm1 (top), Pm5 (middle), and Pm10 (bottom). For each case, the PDFs are shown during the kinematic (orange), intermediate (green), and saturated (purple) phases of magnetic field evolution. These PDFs are computed over multiple independent realizations (at different $t_{\rm ed}$) of the fluctuation dynamo in each of the aforementioned phases. As is evident from the figure, during the kinematic phase, density enhancements play a crucial role in driving the amplification of the magnetic field. Consequently, the strong positive correlation observed in Figure 3 indicates that density variations are also correlated with variations in magnetic pressure. This results in an initial parallel alignment between $\nabla\rho$ and ∇B^2. This trend can be inferred from the PDF values at $\cos(\theta) = 1$. For both Pm1 and Pm5, the density at $\cos(\theta) = 1$ remains close to $\sim$5 across all three phases. However, as the magnetic field continues to be amplified through random stretching, magnetic pressure forces begin to resist further compression of the field lines, leading to the emergence of an antiparallel alignment between the two, consistent with the findings of S. Sur & K. Subramanian (2024). This can again be seen from the density at $\cos(\theta) = -1$, which increases to $\sim$2.5 from its kinematic value.

However, we observe a subtle dependence on Pm, particularly in the saturated phase. As Pm increases, the antiparallel alignment becomes more pronounced, while the parallel alignment gradually diminishes. This behavior is already pronounced for Pm5, where the density at $\cos(\theta) = -1$ rises to $\sim$4 in the saturated phase. For Pm10, the effect is the strongest. In the kinematic phase, the PDF is strongly peaked at $\cos(\theta) = +1$ ($p \simeq 5$), with a much smaller density at $\cos(\theta) = -1$ ($p \simeq 1.5$), indicating that parallel alignment dominates. In the saturated phase, however, this pattern reverses. The density at $\cos(\theta) = +1$ drops to $\sim$2.5, while the same at $\cos(\theta) = -1$ rises to $\sim$4.5. This inversion of the relative endpoint values demonstrates a clear shift from strongly parallel to strongly antiparallel configurations, showing that antiparallel alignment becomes increasingly probable as the dynamo saturates.

Taken together, these results suggest that in the saturated phase, magnetic pressure forces counteract compressive motions more effectively for Pm $>$ 1 than for Pm $=$ 1. For Pm $=$ 10, this effect is significant enough to lead to a steep decline in r_p, as seen in Figure 3.

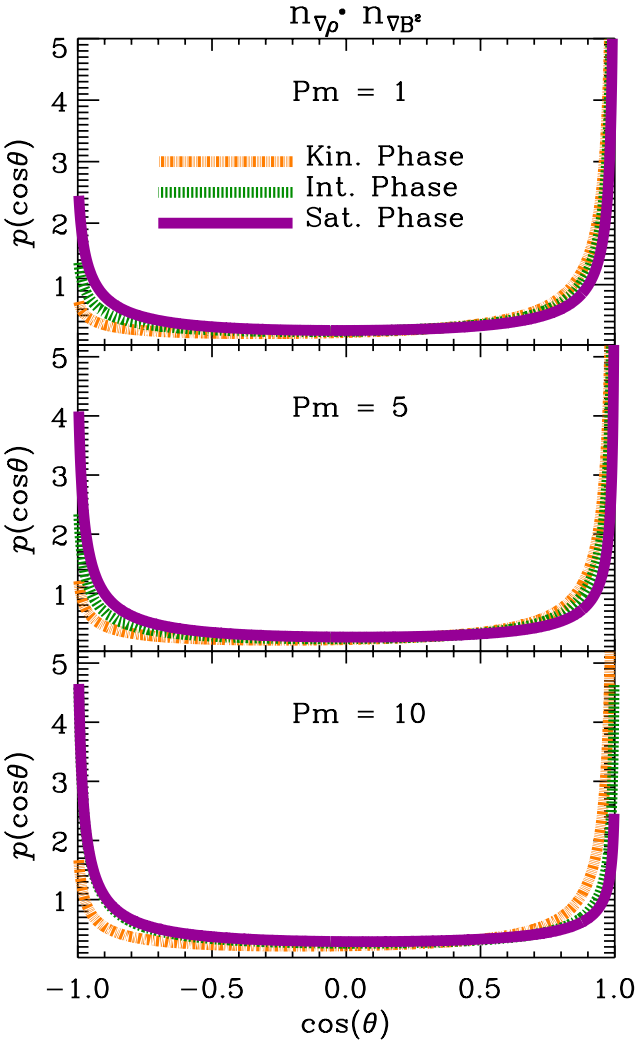

Figure 7. PDFs of the cosine of the angle between $n_{\nabla\rho}$ and $n_{\nabla B^2}$ for runs Pm1 (top), Pm5 (middle), and Pm10 (bottom). For each Pm, the distributions are computed during the kinematic (orange), intermediate (green), and saturated (purple) phases of fluctuation dynamo evolution using multiple independent realizations.

ORCID iDs

Ameya Uday Nagdeo https://orcid.org/0009-0001-8508-3487
Sharanya Sur https://orcid.org/0000-0003-4286-8476
Bhargav Vaidya https://orcid.org/0000-0001-5424-0059

References

Beattie, J. R., Federrath, C., Klessen, R. S., Cielo, S., & Bhattacharjee, A. 2024, arXiv:2405.16626
Benzi, R., Biferale, L., Fisher, R. T., et al. 2008, PhRvL, 100, 234503
Bernet, M. L., Miniati, F., & Lilly, S. J. 2010, ApJ, 711, 380
Bernet, M. L., Miniati, F., Lilly, S. J., Kronberg, P. P., & Dessauges-Zavadsky, M. 2008, Natur, 454, 302
Bevington, P. R., & Robinson, D. K. 2003, Data Reduction and Error Analysis for the Physical Sciences (3rd ed.; McGraw-Hill)
Bhat, P., & Subramanian, K. 2013, MNRAS, 429, 2469
Bournaud, F., Chapon, D., Teyssier, R., et al. 2011, ApJ, 730, 4
Bracco, A., Ntormousi, E., Jelić, V., et al. 2022, A&A, 663, A37
Brandenburg, A., & Subramanian, K. 2005, PhR, 417, 1
Brandenburg, A., & Vishniac, E. T. 2025, ApJ, 984, 78
Chen, J., Lopez-Rodriguez, E., Ivison, R. J., et al. 2024, A&A, 692, A34
Cho, J., & Ryu, D. 2009, ApJL, 705, L90
Cho, J., Vishniac, E. T., Beresnyak, A., Lazarian, A., & Ryu, D. 2009, ApJ, 693, 1449
Collette, Andrew 2013, Python and HDF5 (O'Reilly Media)
Davies, R. L., Förster Schreiber, N. M., Genzel, R., et al. 2021, ApJ, 909, 78
Donnert, J., Vazza, F., Brüggen, M., & ZuHone, J. 2018, SSRv, 214, 122
Eswaran, V., & Pope, S. B. 1988, PhFl, 31, 506
Farnes, J. S., O'Sullivan, S. P., Corrigan, M. E., & Gaensler, B. M. 2014, ApJ, 795, 63
Federrath, C. 2016, JPlPh, 82, 535820601
Federrath, C., Chabrier, G., Schober, J., et al. 2011a, PhRvL, 107, 114504
Federrath, C., Roman-Duval, J., Klessen, R. S., Schmidt, W., & Mac Low, M. M. 2010, A&A, 512, A81
Federrath, C., Sur, S., Schleicher, D. R. G., Banerjee, R., & Klessen, R. S. 2011b, ApJ, 731, 62
Fryxell, B., Olson, K., Ricker, P., et al. 2000, ApJS, 131, 273
Geach, J. E., Lopez-Rodriguez, E., Doherty, M. J., et al. 2023, Natur, 621, 483
Gent, F. A., Mac Low, M.-M., Korpi-Lagg, M. J., & Singh, N. K. 2023, ApJ, 943, 176
Gillespie, D. T. 1996, PhRvE, 54, 2084
Gopalakrishnan, K., & Subramanian, K. 2023, ApJ, 943, 66
Green, A. W., Glazebrook, K., McGregor, P. J., et al. 2010, Natur, 467, 684
Harris, C. R., Millman, K. J., van der Walt, S. J., et al. 2020, Natur, 585, 357
Haugen, N. E., Brandenburg, A., & Dobler, W. 2004, PhRvE, 70, 016308
Haverkorn, M. 2015, ASSL, 407, 483
Hunter, J. D. 2007, CSE, 9, 90
Kaasinen, M., Bian, F., Groves, B., Kewley, L. J., & Gupta, A. 2017, MNRAS, 465, 3220
Kazantsev, A. P. 1968, JETP, 26, 1031
Kluyver, T., Ragan-Kelley, B., Pérez, F., et al. 2016, in Positioning and Power in Academic Publishing: Players, Agents and Agendas, ed. F. Loizides & B. Schmidt (IOS Press), 87
Kraljic, K., Renaud, F., Dubois, Y., et al. 2024, A&A, 682, A50
Kriel, N., Beattie, J. R., Federrath, C., Krumholz, M. R., & Hew, J. K. J. 2025, MNRAS, 537, 2602
Kritsuk, A. G., Norman, M. L., Padoan, P., & Wagner, R. 2007, ApJ, 665, 416
Lian, J., Wang, T., Feng, Q., Huang, Y., & Guo, H. 2025, ApJL, 990, L37
Malik, S., Chand, H., & Seshadri, T. R. 2020, ApJ, 890, 132
Marinacci, F., Vogelsberger, M., Pakmor, R., et al. 2018, MNRAS, 480, 5113
Mignone, A., Bodo, G., Massaglia, S., et al. 2007, ApJS, 170, 228
Pakmor, R., Gómez, F. A., Grand, R. J. J., et al. 2017, MNRAS, 469, 3185
Price-Whelan, A. M., Sipőcz, B. M., Günther, H. M., et al. 2018, AJ, 156, 123
Rincon, F. 2019, JPlPh, 85, 205850401
Rizzo, F., Bacchini, C., Kohandel, M., et al. 2024, A&A, 689, A273
Schekochihin, A. A. 2022, JPlPh, 88, 155880501
Schekochihin, A. A., Cowley, S. C., Taylor, S. F., Maron, J. L., & McWilliams, J. C. 2004, ApJ, 612, 276
Schober, J., Schleicher, D., Federrath, C., Klessen, R., & Banerjee, R. 2012, PhRvE, 85, 026303
Seta, A., Bushby, P. J., Shukurov, A., & Wood, T. S. 2020, PhRvF, 5, 043702
Seta, A., & Federrath, C. 2021a, PhRvF, 6, 103701
Seta, A., & Federrath, C. 2021b, MNRAS, 502, 2220
Seta, A., & Federrath, C. 2022, MNRAS, 514, 957
Shukurov, A. M., & Subramanian, K. 2021, Astrophysical Magnetic Fields: From Galaxies to the Early Universe (Cambridge Univ. Press)
Sokoloff, D., Bykov, A., Shukurov, A., et al. 1998, MNRAS, 299, 189
Subramanian, K., Shukurov, A., & Haugen, N. E. L. 2006, MNRAS, 366, 1437
Sur, S., Bhat, P., & Subramanian, K. 2018, MNRAS, 475, L72
Sur, S., Federrath, C., Schleicher, D. R. G., Banerjee, R., & Klessen, R. S. 2012, MNRAS, 423, 3148
Sur, S., Schleicher, D. R. G., Banerjee, R., Federrath, C., & Klessen, R. S. 2010, ApJL, 721, L134
Sur, S., & Subramanian, K. 2024, MNRAS, 527, 3968
Virtanen, P., Gommers, R., Oliphant, T. E., et al. 2020, NatMe, 17, 261
Wall, J. V., & Jenkins, C. R. 2012, Practical Statistics for Astronomers (Cambridge Univ. Press)
Xu, S., & Lazarian, A. 2016, ApJ, 833, 215
Xu, S., & Lazarian, A. 2021, RvMPP, 5, 2